CrossMark

ORIGINAL ARTICLE

Periodic orbits, manifolds and heteroclinic connections in the gravity field of a rotating homogeneous dumbbell-shaped body

Xiangyu Li[1,2] · Ai Gao[1,2] · Dong Qiao[1,2]

Abstract This paper studies local and global motion in the vicinity of a rotating homogeneous dumbbell-shaped body through the polyhedron model. First, a geometric model of dumbbell-shaped bodies is established. The equilibria points and stabilities thereof are analyzed under different parameters. Then, local motion around equilibrium points is investigated. Based on the continuation method and bifurcation theory, several families of periodic orbits are found around these equilibria. Finally, to better understand the global orbital dynamics of particles around a dumbbell-shaped body, the invariant manifolds associated with periodic orbits are discussed. Four heteroclinic connections are found between equilibria. Using Poincaré sections, trajectories are designed for transfers between different periodic orbits. Those trajectories allow for low-energy global transfer around a dumbbell-shaped body and can be references for designing reconnaissance orbits in future asteroid-exploration missions.

✉ A. Gao
  gaoai@bit.edu.cn

  X. Li
  lixiangy@bit.edu.cn

  D. Qiao
  qiaodong@bit.edu.cn

[1] School of Aerospace Engineering, Beijing Institute of Technology, Beijing 100081, China

[2] Key Laboratory of Autonomous Navigation and Control for Deep Space Exploration, Ministry of Industry and Information Technology, Beijing 100081, China

1 Introduction

Asteroids, considered to be remnant material from the early solar system, have become desirable destinations for deep space exploration in recent years. Valuable information from asteroids about the evolution of the solar system, the formation of planets and the source of life, as well as their potential for human exploration missions, attracts both scientists and engineers. However, missions to asteroids face significant dynamical problems. One of the major challenges to probes is the strong gravitational perturbations caused by the irregular shapes of asteroids. Lack of familiarity with the dynamics of the environment in the vicinity of an asteroid makes it difficult to keep a spacecraft safe around a small body.

To overcome this difficulty, several studies have been conducted in the past. Different asteroid models have been proposed to approximate the gravity field caused by the irregular shape of an asteroid, including but not limited to a tri-axial ellipsoid (Scheeres 1994), a homogeneous cube (Liu et al. 2011a,b), an annular disk (Alberti and Vidal 2007), an elongated segment (Riaguas et al. 2001), a dumbbell-shaped body (Li et al. 2013), a combination of a sphere and an ellipsoid (Feng et al. 2015, 2016), a rotating mass dipole (Zeng et al. 2015) and a polyhedron model (Hudson and Ostro 1994; Yu and Baoyin 2012b; Wang et al. 2015). Of these, the dumbbell-shaped body is an ideal model, consisting of two incomplete spheres and one optional cylinder. By varying the relative position and the size of spheres, this model has the ability to simulate an elongated asteroid, a contact binary or more complicated asteroids, which are suitable approximations for a number of real celestial bodies in the solar system.

Based on the above gravitational models, the motion of a particle in the vicinity of an asteroid has been investigated. The equilibrium points and stability, periodic

orbits (Scheeres et al. 1996; Yu and Baoyin 2013; Wang et al. 2014) and topological structure of motion (Lara and Scheeres 2002; Jiang and Baoyin 2014; Jiang et al. 2014; Feng et al. 2016) around the asteroid have been studied. In particular, based on the dumbbell-shaped model, Li analyzed the equilibrium points and their linear stability for different length-diameter ratios. Additionally, planar periodic orbits around equilibrium points were found.

In this paper, we further investigate the motion around dumbbell-shaped bodies. In particular, we extend the research from local motion around equilibrium points to global motion in the vicinity of a dumbbell-shaped body. The local motion in space is discussed, and additional families of periodic orbits around equilibria are generated by bifurcation theory. Moreover, the invariant manifold associated with orbits is analyzed, which may help to study the low-energy connections between equilibria. With the help of manifolds and Poincaré sections, potential global transfer trajectories around a dumbbell-shaped body are designed. The study of local and global motion can provide a reference to select proper transfer and reconnaissance orbits around small celestial bodies, which is essential to future exploration mission design.

This paper is organized as follows. In Sect. 2, the dumbbell-shaped model is established, the equilibria are calculated, and the critical angular speed is investigated. In Sect. 3, we treat the local motion around equilibria. With the continuation method and bifurcation theory, several families of periodic orbits are generated. The global motion in the vicinity of a dumbbell-shaped body is discussed in Sect. 4. The invariant manifolds associated with periodic orbits are calculated for different extended length-diameter ratios and orbit amplitudes. By introducing the Poincaré section, the heteroclinic connections around dumbbell-shaped bodies are analyzed. Finally, several global transfer trajectories are designed to demonstrate the potential application to small-body exploration.

2 Dynamic equation in dumbbell-shaped model

2.1 The dumbbell-shaped model

In this paper, a dumbbell-shaped body is employed for dynamic research. The model is the combination of two incomplete spheres and an optional cylinder, as shown in Fig. 1.

For simplicity, the radii of the two spheres are the same, denoted as R. The radius of the cylinder is half that of the sphere, $R_c = R/2$. There is one additional important parameter that describes the shape of the model: the length-diameter ratio $m = L/2R$, where L is distance between the centers of the two spheres. It is easy to show that $m \leq \sqrt{3}/2$ describes two spheres in contact, which is analogous to a
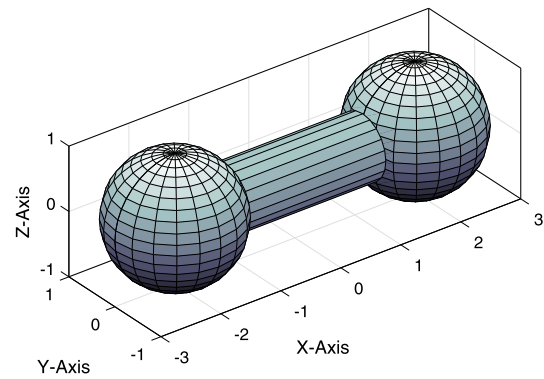

Fig. 1 The dumbbell-shaped model

contact binary asteroid. The cylinder is used when $m > \sqrt{3}/2$; the height of cylinder is $H = L - 2\sqrt{R^2 - R_c^2}$. The special case of $m = 0$ represents a single sphere.

2.2 Gravitational potential

We assume that the dumbbell-shaped body is homogeneous. The gravitational potential of a dumbbell-shaped body can be calculated by the polyhedron method (Werner and Scheeres 1996). The incomplete spheres and cylinder are meshed into a set of tetrahedrons. The gravitational potential at an external point P due to each part can be calculated by Eq. (1).

$$U = \frac{1}{2}G\sigma \sum_{e \in edges} \mathbf{r}_e \cdot \mathbf{E}_e \cdot \mathbf{r}_e \cdot L_e - \frac{1}{2}G\sigma \sum_{f \in faces} \mathbf{r}_f \cdot \mathbf{F}_f \cdot \mathbf{r}_f \cdot \omega_f$$

(1)

where L_e and ω_f represent the line factor and the face factor, respectively. $\mathbf{r}_e$ is a vector from a point on edge e to P. $\mathbf{E}_e$ and $\mathbf{F}_f$ are the direction matrices of edge e and the embodied face f. The potential of the dumbbell-shaped body at point P can be obtained by summing the potentials of the three parts. The attraction and gravity gradient of the polyhedron can also be obtained by Eqs. (2) and (3), which are applied in the following sections.

$$\nabla U = -G\sigma \sum_{e \in edges} \mathbf{E}_e \cdot \mathbf{r}_e \cdot L_e + G\sigma \sum_{f \in faces} \mathbf{F}_f \cdot \mathbf{r}_f \cdot \omega_f$$

(2)

$$\nabla\nabla U = G\sigma \sum_{e \in edges} \mathbf{E}_e \cdot L_e - G\sigma \sum_{f \in faces} \mathbf{F}_f \cdot \omega_f$$ (3)

2.3 The equilibria and their stability

The dumbbell-shaped body is assumed to be rotating uniformly around its maximum moment-of-inertia axis with angular velocity ω. Normally, the motion of a third particle is

Table 1 Location, existence and stabilities of periodic orbits for the equilibrium points

Model	Equilibrium	x	y	Linear stability[*]
I	$\mathbf{E}_x$	±2.51577234	0	U
	$\mathbf{E}_y$	0	±2.42416646	LS
II	$\mathbf{E}_x$	±2.93537532	0	U
	$\mathbf{E}_y$	0	±2.59233070	U
III	$\mathbf{E}_x$	±3.81066268	0	U
	$\mathbf{E}_y$	0	±2.35860180	U
IV	$\mathbf{E}_y$	±5.59691038	0	U
	$\mathbf{E}_y$	0	±5.41947608	LS

[*]Note: U = unstable LS = Linearly stable

established in the body-fixed frame whose Z-axis is aligned with the rotation axis, and whose X- and Y-axes coincide with two other symmetrical axes of the body. The centers of the two spheres are located at the X-axis.

In the rotating frame, the equation of motion of a particle is given as,

$$\ddot{x} - 2\omega\dot{y} = \omega^2 x + U_x$$
$$\ddot{y} + 2\omega\dot{x} = \omega^2 y + U_y \qquad (4)$$
$$\ddot{z} = U_z$$

where U_x, U_y, U_z are components of Eq. (1) along the respective axes. The results of Eq. (4) are related only to the ratio between the square of the rotational speed and the density of the body: $\tau = \omega^2/\rho$. Therefore, we define a normalized angular speed $\omega' = \sqrt{\omega^2/G\rho}$. In the new system, the gravity constant G' and the density ρ' of the model are equal to 1. That is, any property of motion in the system $S' = \{\omega', G', \rho', R\}$ is equivalent to the original system $S = \{\omega, G, \rho, R\}$. The radii of sphere R is taken as the length unit. The normalized equation can be written as,

$$\ddot{x} - 2\omega'\dot{y} = \omega'^2 x + U_x$$
$$\ddot{y} + 2\omega'\dot{x} = \omega'^2 y + U_y \qquad (5)$$
$$\ddot{z} = U_z$$

Setting $\dot{x} = \ddot{x} = \ddot{y} = \dot{y} = \dot{z} = \ddot{z} = 0$, the equilibrium points of the dumbbell-shaped body can be obtained. Their stability can be determined by the eigenvalues of the characteristic equation. The equilibrium is stable if no eigenvalue has a positive real part; otherwise, the equilibrium is unstable. According to a previous study (Li et al. 2013), an equilibrium along the X-axis is always unstable, while equilibrium points along the Y-axis are conditionally stable. The stability at a certain angular speed has been investigated and the corresponding critical length-diameter ratio m_{cr} was found. Here, we focus on determining the critical length-diameter ratio m_{cr} with different angular velocities.

The normalized angular velocity ω' is allowed to change from 0.1 to 1. For each ω', the critical length-diameter ra-
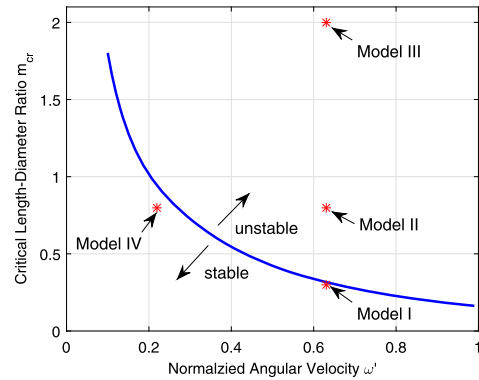

Fig. 2 The relation between normalized angular velocity ω' and critical length-diameter ratio m_{cr}

tio is calculated that satisfies the multiple eigenvalues in the characteristic equation. The result is shown in Fig. 2.

As shown in Fig. 2, the curve divides the region into two parts. In the upper region, the equilibria along the Y-axis are unstable, while the lower region is the stable area. It is clear that the critical length-diameter ratio decreases as the normalized angular speed increases. Considering the definition of normalized angular speed, it is concluded that an equilibrium with a high spin speed or low-density body is usually unstable unless the body is close to a sphere.

To systematically discuss the motion in the vicinity of a dumbbell-shaped model, four models are analyzed below: I. $\omega' = 0.63, m = 0.3$, II. $\omega' = 0.63, m = 0.8$, III. $\omega' = 0.63, m = 2$, IV. $\omega' = 0.22, m = 0.8$. From Fig. 2, models II and III are larger than the corresponding critical length-diameter ratio m_{cr}, while I and IV are smaller than m_{cr}. Hence, the equilibrium points along the Y-axis are unstable for II and III and stable for I and IV. The position and linear stability of equilibrium for each situation are listed in Table 1.

3 Local motion around the equilibria of a dumbbell-shaped body

If we put the center of a frame at any equilibrium and perform a small perturbation (ξ, η, ζ), the linear perturbation

equation can be written as:

$$\ddot{\xi} - 2\omega'\dot{\eta} = U_{xx}^E\xi + U_{xy}^E\eta + U_{xz}^E\zeta$$

$$\ddot{\eta} + 2\omega'\dot{\xi} = U_{yx}^E\xi + U_{yy}^E\eta + U_{yz}^E\zeta \qquad (6)$$

$$\ddot{\zeta} = U_{zx}^E\xi + U_{zy}^E\eta + U_{zz}^E\zeta$$

The characteristic equation of Eq. (6) can be written in the following form:

$$\begin{vmatrix} \lambda^2 - U_{xx}^E & -2\omega'\lambda - U_{xy}^E & U_{xz}^E \\ 2\omega'\lambda - U_{xy}^E & \lambda^2 - U_{yy}^E & U_{yz}^E \\ U_{xz}^E & U_{yz}^E & \lambda^2 - U_{zz}^E \end{vmatrix} = 0 \qquad (7)$$

Due to the symmetry of the model, $U_{xy}^E = U_{yx}^E = 0$, $U_{yz}^E = U_{zy}^E = 0$, $and\, U_{xz}^E = U_{zx}^E = 0$. Equation (7) can be simplified as:

$$\left(\lambda^2 - U_{zz}^E\right)\left[\lambda^4 + \left(4\omega'^2 - U_{xx}^E - U_{yy}^E\right)\lambda^2 + U_{xx}^E U_{yy}^E\right] = 0 \qquad (8)$$

where λ denotes the eigenvalues of Eq. (6). The value of λ not only defines the stability of equilibrium points but also determines the mode of perturbation motion around equilibria. Planar periodic orbits around equilibria have been investigated previously (Li et al. 2013). Here, we extend them to the spatial situation.

3.1 Local motion around an equilibrium

Case 1. Local motion around an equilibrium along the X-axis

The eigenvalues for E_x in a dumbbell-shaped body have the form $\pm\alpha, \pm i\beta_j$ $(j = 1, 2)$. Hence, the general solution of the linearized equation can be expressed as (Wang et al. 2014):

$$\xi = d_1 e^{\alpha t} + d_2 e^{-\alpha t} + d_3 \cos\beta_1 t + d_4 \sin\beta_1 t$$

$$\eta = \kappa_1\left(d_1 e^{\alpha t} - d_2 e^{-\alpha t}\right) - \kappa_2\left(d_3 \sin\beta_1 t - d_4 \cos\beta_1 t\right) \qquad (9)$$

$$\zeta = d_5 \cos\beta_2 t + d_6 \sin\beta_2 t$$

where $\kappa_1 = \frac{1}{2\omega'}(\alpha - \frac{U_{xx}^E}{\alpha_1})$, $\kappa_2 = \frac{1}{2\omega'}(\beta_1 + \frac{U_{xx}^E}{\beta_1})$. Motion along the z-axis is decoupled from motion in the xy-plane. Therefore, two types of periodic orbits can be found near E_x. One is in the xy-plane with period $T_1 = 2\pi/\beta_1$ as discussed previously; the other is the out-of-plane motion with period $T_2 = 2\pi/\beta_2$. Equation (9) provides a proper initial guess for periodic orbits. Based on a differential correction, the accurate result can be obtained as shown in Fig. 3.

The perturbation motion around equilibria can also be described in matrix form,

$$X(t) = \Phi(t, t_0)X(t_0) \qquad (10)$$
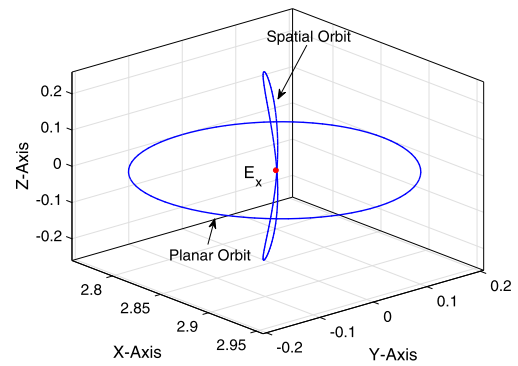

Fig. 3 Periodic orbits around E_x in model II

Table 2 Stabilities and periods of orbits around E_x

Model	Type	Period	Stability index
I	Planar	9.399	6.771
	Spatial	9.653	7.282
II	Planar	8.099	34.356
	Spatial	8.529	43.194
III	Planar	6.816	230.744
	Spatial	7.226	336.088
IV	Planar	27.049	6.193
	Spatial	27.701	6.578

where $X(t_0)$ and $X(t)$ are the perturbations at the initial time t_0 and time t, respectively. $\Phi(t, t_0)$ is the state transition matrix. In particular, the periodic orbit satisfies $X(T) = X(t_0)$. The state transition matrix for a periodic orbit is called Monodromy matrix $M = \Phi(T, t_0)$. Normally, the stability of an orbit is defined by a stability index,

$$\upsilon = \frac{1}{2}\left(|\lambda_{\max}| + \frac{1}{|\lambda_{\max}|}\right) \qquad (11)$$

where $\lambda_{\max}$ is the maximum eigenvalue of the monodromy matrix. If $\upsilon > 1$, the period orbit is unstable. The larger the value of υ, the more easily the orbit diverges. Periodic orbits were investigated for the dumbbell-shape models with different parameters. Table 2 lists the stabilities and periods of orbits with the same amplitude ($\Delta\xi(\zeta) = 0.1$).

As shown in Table 2, the periods and stabilities of periodic orbits around E_x are influenced by both the angular speed ω' and length-diameter ratio m. Two types of periodic orbits are unstable under all circumstances. On one hand, when increasing the length-diameter m, the orbital periods of planar and spatial orbits decrease slowly but the stability indexes increase rapidly. On the other hand, the orbital periods and stability of an orbit increase with the decrease of the angular velocity. Additionally, the spatial orbit is more unstable than the planar orbit in the same model.
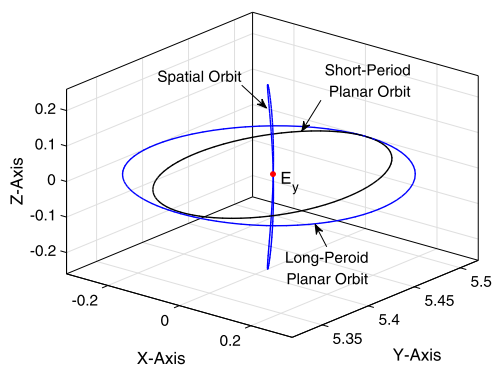
Fig. 4 Periodic orbits around E_y in model IV

Fig. 5 Periodic orbits around E_y in model II

Case 2. Local motion around an equilibrium along the Y-axis

The local motion around equilibrium E_y of a dumb-bell-shaped body depends on the stability of E_y. If the length-diameter ratio m is smaller than m_{cr}, the equilibrium is stable. The eigenvalues for E_y have the form $\pm i\beta_j$ ($j = 1, 2, 3$). Hence, the general solution of the linearized equation can be written as

$$\xi = d_1 \sin(\beta_1 t + \varphi_1) + d_2 \sin(\beta_2 t + \varphi_2)$$
$$\eta = \kappa_1 d_1 \cos(\beta_1 t + \varphi_1) + \kappa_2 d_2 \cos(\beta_2 t + \varphi_2) \quad (12)$$
$$\zeta = d_3 \cos(\beta_3 t + \varphi_3)$$

where $\kappa_1 = \frac{1}{2\omega'}(\beta_1 + \frac{U_{xx}^E}{\beta_1})$, $\kappa_2 = \frac{1}{2\omega'}(\beta_2 + \frac{U_{xx}^E}{\beta_2})$. Three types of periodic orbits can be found near equilibria. Two are in the xy-plane and the other is out-of-plane. Their periods are $T_j = 2\pi/\beta_j$ ($j = 1, 2, 3$), respectively. The numerical results of periodic orbits are shown in Fig. 4.

For a dumbbell-shaped body with a length-diameter ratio larger than m_{cr}, E_y becomes unstable. The forms of the eigenvalues are $\pm\alpha \pm i\beta_1$ and $\pm\beta_2$. The linearized equations of motion near equilibria are

$$\xi = e^{\alpha t}(C_1 \cos\beta_1 t + C_2 \sin\beta_1 t)$$
$$\quad + e^{-\alpha t}(C_3 \cos\beta_1 t + C_4 \sin\beta_1 t)$$
$$\eta = e^{\alpha t}(D_1 \cos\beta_1 t + D_2 \sin\beta_1 t) \quad (13)$$
$$\quad + e^{-\alpha t}(D_3 \cos\beta_1 t + D_4 \sin\beta_1 t)$$
$$\zeta = C_5 \cos\beta_2 t + C_6 \sin\beta_2 t$$

where D_i are functions of C_i ($i = 1, 2, 3, 4$). Only one type of periodic orbit exists, as shown in Fig. 5.

The periods and stabilities of periodic orbits in different models are listed in Table 3 ($\Delta\xi(\zeta) = 0.1$).

As shown in Table 3, the stable equilibria have stable periodic orbits in both the planar and spatial dimensions. Similar to orbits around E_x, the stability indices of spatial orbits increase as m increases, but the periods remain nearly unchanged.
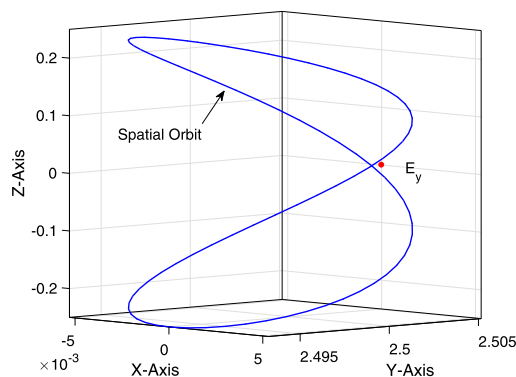
Table 3 Stabilities and periods of orbits around E_y

Model	Type	Period	Stability index
I	Planar I	12.678	1
	Planar II	16.177	1
	Spatial	9.981	1
II	Planar	9.528	7.775
III	Planar	9.978	32.984
IV	Planar I	33.241	1
	Planar II	55.825	1
	Spatial	28.566	1

3.2 Continuation method for orbit families

The linearized equation can provide initial guesses for orbits close to the equilibria. However, it fails when the perturbation is large. In that case, the continuation method is adopted to generate a family of orbits. In this paper, the pseudo-arc-length continuation is employed (Doedel et al. 2007). A new member of the family X_i is generated from the previous converged solution X_{i-1} with a step along the characteristic direction ΔX.

Taking the periodic orbit along the X-axis as an example, according to symmetry, the converged solution satisfies

$$X_{i-1}^{\eta}\left(\frac{T}{2}\right) = 0, \qquad X_{i-1}^{\dot{\xi}}\left(\frac{T}{2}\right) = 0, \qquad X_{i-1}^{\dot{\zeta}}\left(\frac{T}{2}\right) = 0 \quad (14)$$

The characteristic direction ΔX_i should satisfy

$$X_i^{\eta}\left(\frac{T}{2} + \Delta t_i\right) = 0, \qquad X_i^{\dot{\xi}}\left(\frac{T}{2} + \Delta t_i\right) = 0,$$
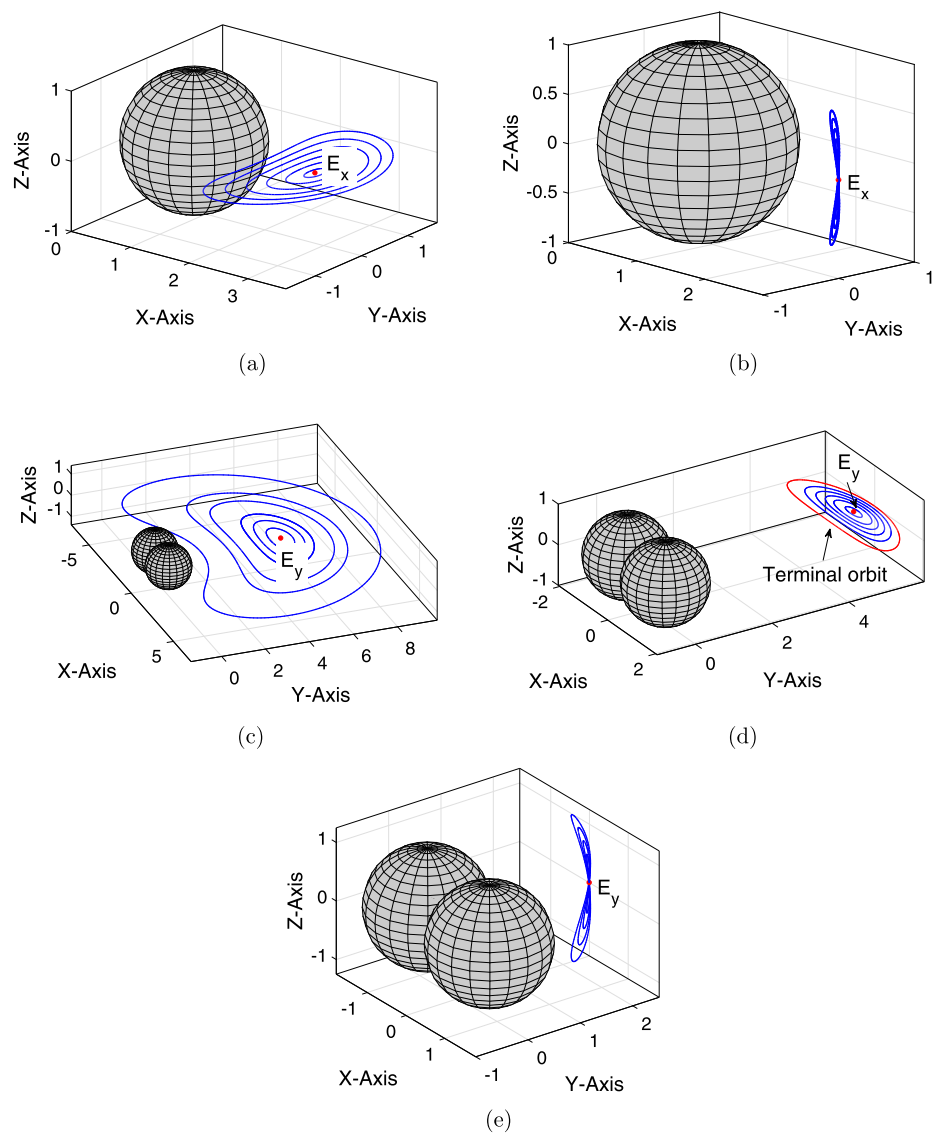$$X_i^{\dot{\zeta}}\left(\frac{T}{2} + \Delta t_i\right) = 0 \quad (15)$$

where Δt_i is the half value of the period, and

$$\Delta X_i = [\Delta\xi \quad 0 \quad \Delta\zeta \quad 0 \quad \Delta\dot{\eta} \quad 0].$$

Equation (15) can be written in matrix form as

$$\left.\frac{\partial X}{\partial X_0}\right|_{T/2} \Delta X_i + \left.\frac{\partial X}{\partial t}\right|_{T/2} \Delta t_i = 0 \quad (16)$$

Fig. 6 Orbit Families around equilibria in Model IV (**a**) E_x planar orbits (**b**) E_x vertical orbits (**c**) E_y short-period orbits (**d**) E_y long-period orbits (**e**) E_y vertical orbits

An additional constraint, $|\Delta X_i|^2 + |\Delta t_i|^2 = 1$, is added to keep the solution unique. A step size Δs is chosen to generate a new guess for a differential correction:

$$X_i = X_{i-1} + \Delta X_i \Delta s \qquad (17)$$

The pseudo-arc-length continuation provides a better initial guess than the traditional continuation method and increases the convergence. Based on the continuation, a family of periodic orbits are produced as shown in Fig. 6.

All orbits can extend to the surface of the dumbbell-shaped body except the long-period orbit around stable E_y, where the orbit suddenly disappears in space. Figure 6(d) shows the terminal orbit.

3.3 Periodic orbits via bifurcation

Based on the linear perturbation equations above, several types of periodic orbits can be found and orbit families generated. However, more complex periodic orbits such as the "Halo" type orbit in the

Circular Restricted Three Body Problem (CRTBP) cannot be found by such methods. Three methods have been used to search for periodic orbits. One is the grid search, in which six-dimensional states $(x, y, z, \dot{x}, \dot{y}, \dot{z})$ and the period T are regarded as searching parameters in a meshed grid to find a periodic solution. Yu has used this to find 29 families of periodic orbits around 216 Kleopatra (Yu and Baoyin 2012a). This method can search for orbits systematically, but it is time-consuming, especially for polyhedron models. The second method requires a high-order analytical solution as in the CRTBP. However, it is difficult to obtain a high-order derivate by the polyhedron method. Therefore, the third method, bifurcation, is employed to find additional periodic orbits in the vicinity of a dumbbell-shaped model.

Bifurcation is a common phenomenon in nonlinear dynamic systems. In the context of periodic orbits, bifurcation means a change in stability of orbits or the location of eigenvalues in the complex plane (Chappaz 2015). One of the characteristics of bifurcation is the existence of a new family of orbits that intersects the known family at the bifurcation point; this facilitates the search for periodic orbit families. Bifurcation has been studied analytically

for asteroids by Yu and applied to asteroid 216 Kleopatra (Jiang et al. 2015). Here, we extend it to search for periodic orbits for a singular polyhedron body.

Based on continuation, the motion of an eigenvalue for planar orbits around E_x is shown in Fig. 7.

As shown in Fig. 7, initially, the original orbit has two eigenvalues equal to 1, and two of the eigenvalues lie on the unit circle. Two other eigenvalues are located on the real axis. As the orbit amplitude increases, two complex eigenvalues converge at 1 and split on the real axis into a real reciprocal pair, which indicates a tangent bifurcation (Campbell 1999). By bisection and the continuation method, the accuracy of the bifurcation orbit can be calculated numerically. If we denote the bifurcation eigenvalue $\lambda_{bi} = -1$ and the corresponding eigenvector as $V(\lambda_{bi})$ and $V(\lambda_{bi}^*)$, the average eigenvector is defined as

$$V = \left[V(\lambda_{bi}) + V(\lambda_{bi}^*) \right]/2 \qquad (18)$$

The initial guess of a new orbit family can be obtained as $X^{new} = X_{bi} + \Delta s \cdot V$, where X_{bi} is the initial state of the periodic orbit at bifurcation points, and Δs is an arbitrary step size. Once the first orbit of a new type is generated, the continuation method is used to fill up the whole family. By bifurcation, two types of periodic orbits are found around E_x, as shown in Fig. 8.

Figure 9 marks the bifurcation orbits from the original orbit family. Those two types of orbits are analogous to axial orbits and Halo orbits in the CRTBP.

The eigenvalues of vertical orbits in E_x have also been investigated. The location of eigenvalues is the same as for a planar orbit. However, no bifurcation occurs when we increase the Z-axis amplitude.
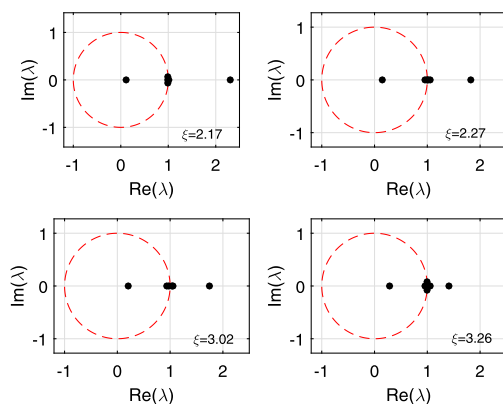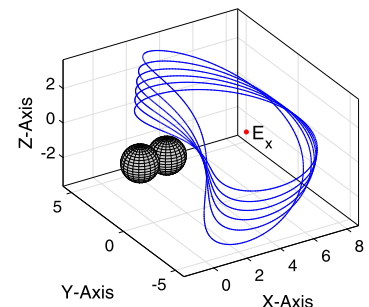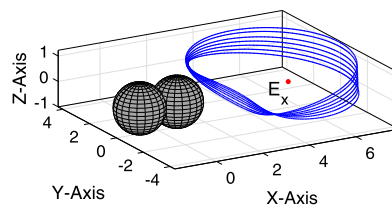
The same process is applied to periodic orbits around E_y. The eigenvalues of a vertical periodic orbit around stable and unstable equilibria are shown in Fig. 10. The vertical orbits around stable equilibria have 2 pairs of complex eigenvalues lying on the unit circle and one pair of unity, while orbits around unstable equilibria have two pairs of eigenvalues in the complex plane. For both types of orbits, no bifurcation occurs even if the amplitude ζ is as large as 3. Therefore, no new orbit family is generated from vertical orbits.

For stable E_y, the bifurcation in two types of planar orbits is discussed further. The long-period orbits occur in secondary Hopf-bifurcation, in which two pairs of complex eigenvalues converge on the unit circle and split into the complex plane, as shown in Fig. 11. The secondary Hopf-bifurcation changes the stability of motion, which results in the disappearance of the long-period orbit (Fig. 6(d)).

The bifurcation for a short-period orbit is complicated. With increasing amplitude, the eigenvalue successively incurs period-doubling bifurcation (the eigenvalue converges to -1) and tangent bifurcation (the eigenvalue converges to 1). The motion of characteristic value for model IV is shown in Fig. 12.

According to bifurcation theory, the doubling bifurcation will generate a new orbit family possessing a period double that of the original family (Iooss and Joseph 1977). Based on new initial guesses, multiple-cycle orbits are found near E_y, as shown in Fig. 13(a) and (b). Additionally, the tangent bifurcation for a short-period orbit produces a new kind of asymmetrical period orbit. Asymmetrical correction schemes are adopted to find the numerical result (Grebow 2006), as shown in Fig. 13(c). For both long- and short-period orbits around E_y, no spatial orbits are generated from planar orbits as in E_x.
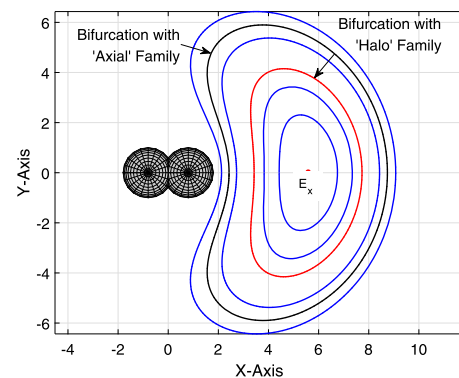

Fig. 7 Motion of characteristic value for planar orbits around E_x (model II)

Fig. 9 Bifurcation orbits in the original orbit family

Fig. 8 Two types of periodic orbits around E_x from the bifurcation (model II)
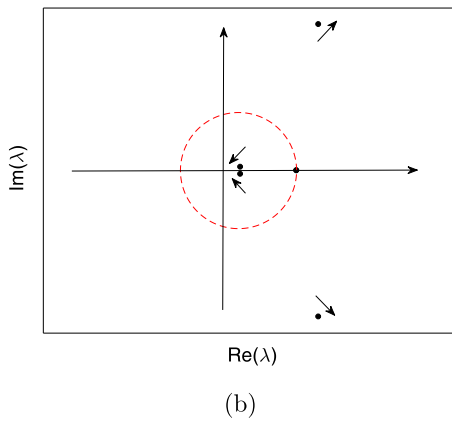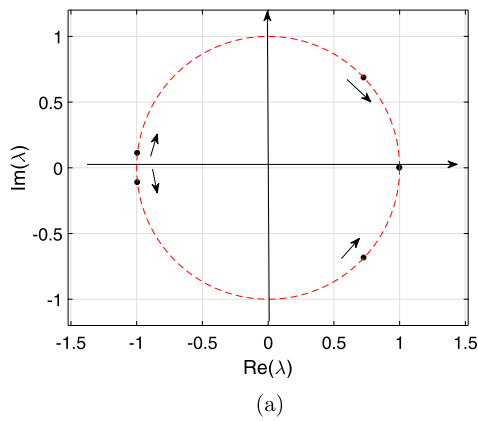
(a)

(b)

Fig. 10 Characteristic values for vertical orbits around E_y (**a**) Stable equilibrium point (model IV) (**b**) Unstable equilibrium point (model II)
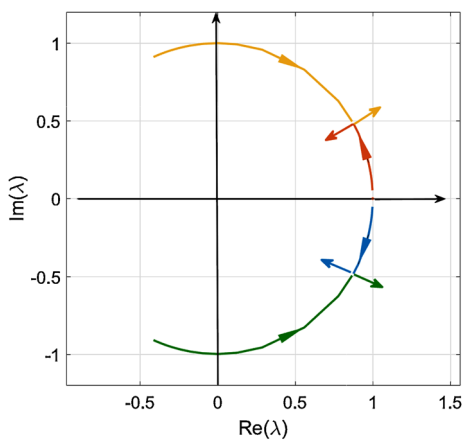

Fig. 11 Hopf-bifurcation for long period orbits (model IV)

4 Global motion in the vicinity of a dumbbell-shaped body

4.1 Invariant manifolds associated with periodic orbits for a dumbbell-shaped body

The invariant manifold is an important property for periodic orbits around equilibria, especially for unstable periodic orbits. An
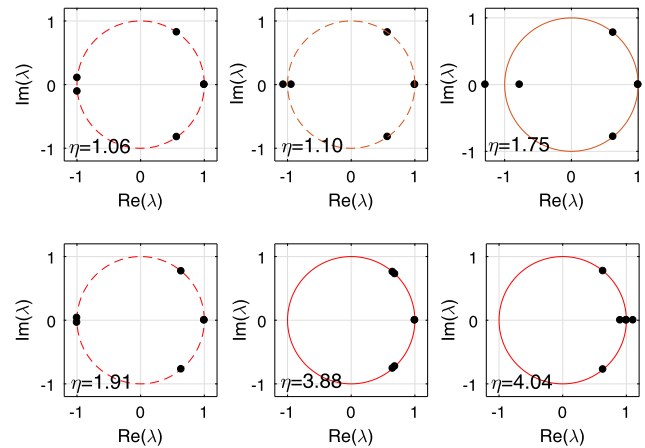
Fig. 12 Motion of characteristic value for short orbits around E_y (model IV)

invariant manifold can be defined as an m-dimensional surface embedded in $\mathbb{R}^n$ ($m < n$). From nonlinear dynamics theory, there are two types of invariant manifolds: unstable manifolds and stable manifolds. The unstable manifold includes the set of all possible trajectories that diverge from a nominal orbit if it was perturbed in an unstable direction of orbits, while the stable manifold is the set of all possible trajectories that asymptotically approach the orbit along a stable direction. The stable and unstable directions can be determined by the Monodromy matrix of a periodic orbit.

Here, we analyze the manifold of an unstable orbit around E_x in the vicinity of a dumbbell-shaped body. The manifold picks up 100 points uniformly from a periodic orbit and generates stable and unstable manifolds forward or backward to the plane $X = 0$. The invariant manifold associated with planar and spatial orbits is shown in Fig. 14.

As illustrated in Fig. 14, there are two branches of stable manifolds (red) and two branches of unstable manifolds (blue). One branch of the stable (unstable) manifolds extends along the positive y-direction and the other stretches to the negative y-direction. The stable and unstable manifolds are symmetric with respect to the X-axis. Moreover, manifolds from E_{-x} are anti-symmetric to manifolds from E_x. In that case, the stable and unstable manifolds are calculated for one quadrant, and the other part can be obtained by symmetry and anti-symmetry. For convenience, the closer branch is called the inner manifold and the branch away from the body is called the outer manifold. The impacts of the orbit amplitude and the length-diameter ratio are investigated as follows.

4.2 Parametric analysis for invariant manifolds

To systematically understand the global motion near the equilibria, the influence of orbit amplitude ξ and length-diameter ratio m on invariant manifolds is investigated. Here, we take a planar orbit as example. Relevant results are shown in Fig. 15.

As shown in Fig. 15, the orbit amplitude ξ has a great impact on the size and direction of the manifold. With the increase of amplitude, the size of the manifold tube increases. Inner and outer manifolds may overlap with each other. Unlike in the CRTBP, the manifold near a dumbbell-shaped body system has nearly the same size as the center body (seen in Fig. 14 and 15). Therefore, the

Fig. 13 Three types of periodic orbits around E_y from bifurcation (model IV) (**a**) Multiple-cycle orbit (**b**) Multiple-cycle orbit (**c**) Asymmetrical period orbit

(a)
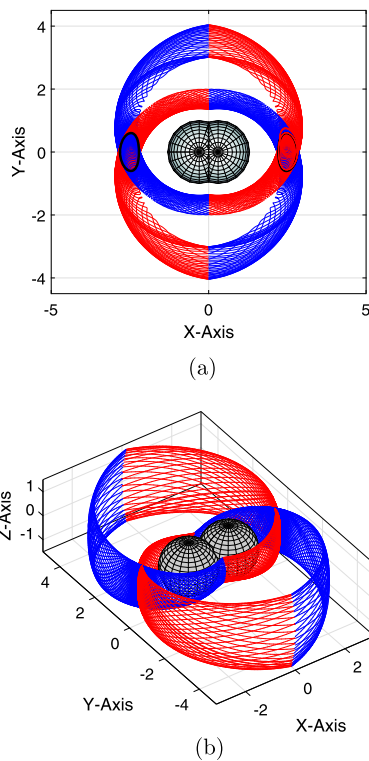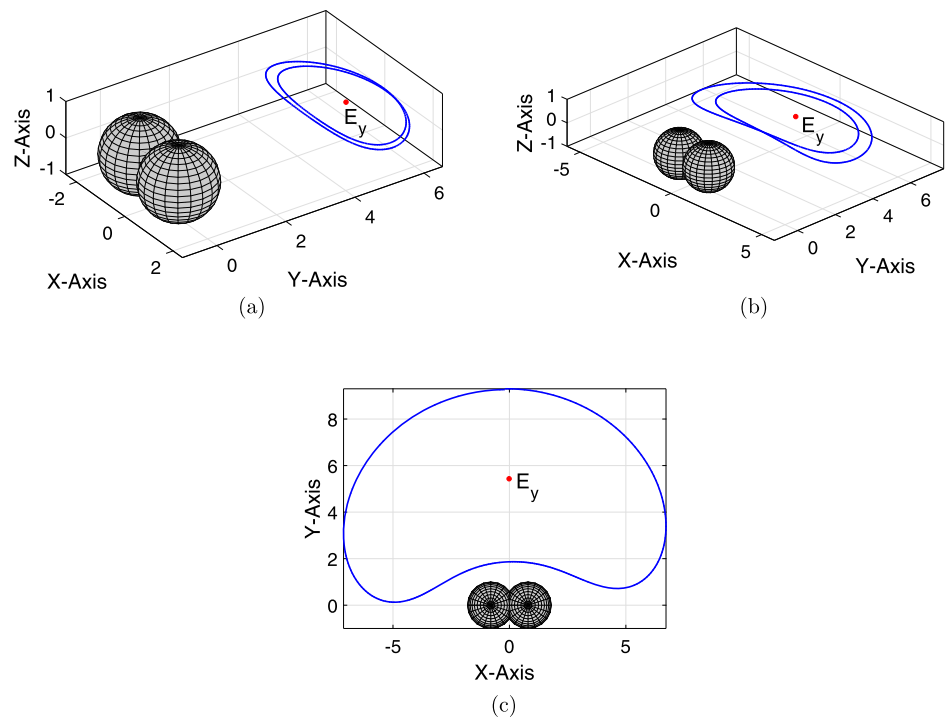

(b)

(c)

(a)

(b)

Fig. 14 Invariant manifold associated with periodic orbit for dumbbell-shaped body (**a**) Planar orbit in model I (**b**) Vertical orbit in model II

inner manifold may touch the surface of a dumbbell-shaped body when the amplitude is large.

Increasing the length-diameter ratio m has the same effect as the amplitude, as shown in Fig. 16, where models II and III are shown

with particular cases $\xi = 0.2$. The inner manifold comes close to the center body as the relative distance between the two spheres increases. In particular, only the outer manifold exists for model III; the inner manifold totally intersects with the model before it crosses the plane $x = 0$.

4.3 Heteroclinic connection between E_x and E_{-x}

As discussed above, there are two branches of stable and unstable manifolds for each orbit around equilibria E_x. That is, at most four heteroclinic connections exist between two equilibria. Each direction has two channels. Spacecraft in periodic orbits can transfer from one equilibrium to the other with limited energy and achieve global exploration of the small body.

To study the low-energy transfer, two Poincaré sections are set as:

$$\begin{cases} U_1 : x = 0, & y > 0, \ \dot{x} > 0 \\ U_2 : x = 0, & y > 0, \ \dot{x} < 0 \end{cases} \quad (19)$$

The black lines in Fig. 15(a) show the sections. The projections for stable and unstable manifolds in these sections are shown in Figs. 17 and 18 for models I and II. The manifolds for different amplitudes are investigated separately.

It is clear that the projection of some stable manifolds overlap with the projection of unstable manifolds on the Poincaré section, which means there are heteroclinic connections between two equilibria points. In particular, if the point of intersection corresponds to an equal-amplitude orbit with the same orbital energy, the connection is a zero-energy transfer. Otherwise, a small energy increment is needed at the intersection point to accommodate the change in velocity.

Comparing models I and II, with the increase of m, the projections of the stable and unstable manifolds in the Poincaré section gradually separate, which means a velocity increment is needed

Fig. 15 Invariant manifold with
different orbit amplitudes
(model I) (**a**) $\xi = 0.2$
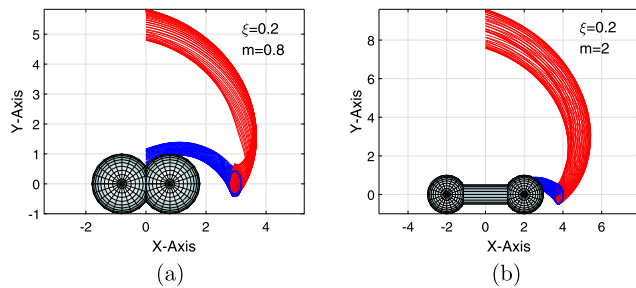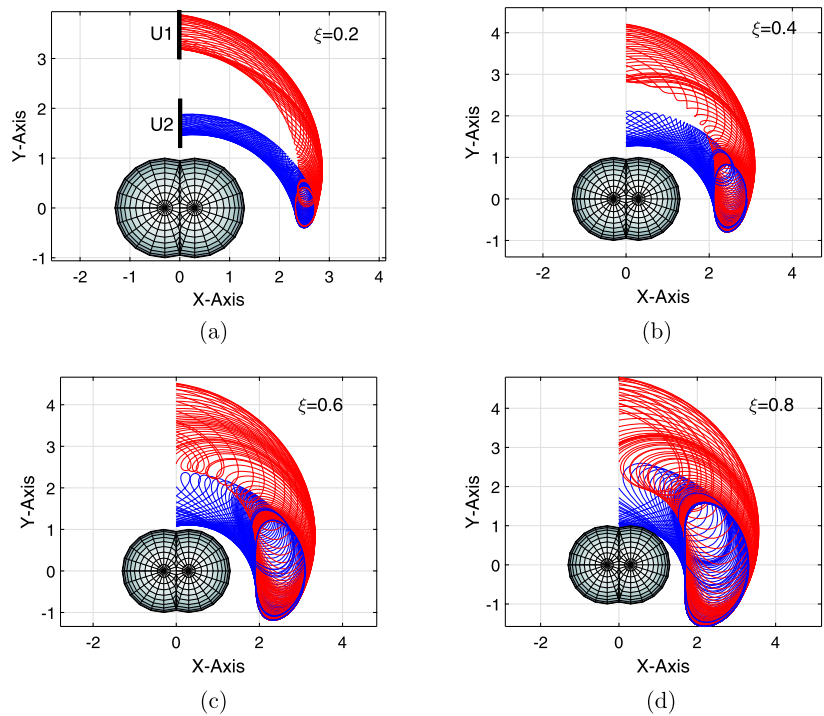(**b**) $\xi = 0.4$ (**c**) $\xi = 0.6$
(**d**) $\xi = 0.8$

(a)

(b)

(c)

(d)

(a)

(b)

Fig. 16 Invariant manifold with different length-diameter ratios (**a**) Model II (**b**) Model III

Fig. 17 Poincaré section for model I

Fig. 18 Poincaré section for model II

clinic connection is applied from E_{-x} to E_x. No extra velocity is needed at the intersection point ($x = 0$). In Fig. 19(b), the spacecraft transfers from a large-amplitude orbit around E_x to a small one around E_{-x}. The velocity increment is only 0.02 on a normalized scale.

Moreover, through two heteroclinic connections, it is possible to transfer the spacecraft between different amplitude orbits around the same equilibria, as shown in Fig. 20. The spacecraft transfers from a small-amplitude orbit to a large-amplitude large-amplitude orbit around E_{-x}. At least one impulse is required during the transfer.

4.4 Heteroclinic connection between E_x and E_y

The above connections focus on the transfer between equilibria along the X-axis. Here, we discuss the transfer between E_x and E_y. Due to the stability of E_y, the invariant manifold cannot be employed to heteroclinic connections for stable periodic orbits. In that case, one-impulse transfers are investigated between a periodic orbit around E_y and a stable or unstable manifold from a periodic orbit around E_x. The Poincaré map for a periodic orbit and invariant manifold is shown in Fig. 21.
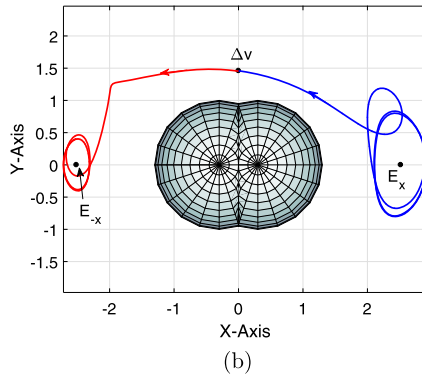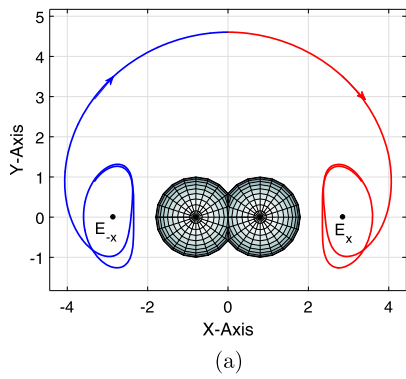
to complete the transfer. Low-energy transfers exist only in large-amplitude manifolds.

Based on the Poincaré section, heteroclinic transfers between two equilibria along the X-axis are shown in Fig. 19. In Fig. 19(a), the transfer is between equal-amplitude orbits. The outer hetero-

(a)

(b)

Fig. 19 Heteroclinic connection between E_x (**a**) Equal-amplitude transfer in model I (**b**) Transfer between different amplitudes in model II
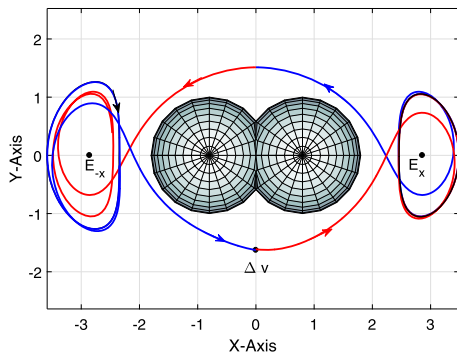

Fig. 20 Transfer between different amplitude orbits (model II)

Fig. 21 Poincaré section for E_y periodic orbit

Fig. 22 Heteroclinic connection between E_x and E_y

Fig. 23 Transfer between different amplitude orbits by the E_y periodic orbit

As shown in Fig. 21, the projection of a periodic orbit in the Poincaré section $Y - V_y$ is a line that coincides with the X-axis. Therefore, the invariant manifold that satisfies $V_y = 0$ is selected as a candidate. The spacecraft will execute one impulse when it crosses the $X = 0$ plane to complete the transfer. Figure 22 shows one of the examples in model I. Generally, the heteroclinic connection between E_x and E_y costs a larger velocity increment than the heteroclinic connection between E_x. However, velocity is not the key factor for a small celestial body. The transfer in Fig. 22 requires a normalized velocity maneuver change of 0.17, which is small on a real scale.

The periodic orbit around E_y can connect with two periodic orbits simultaneously. In that case, the spacecraft can also achieve transfer between different amplitudes by the path of unstable
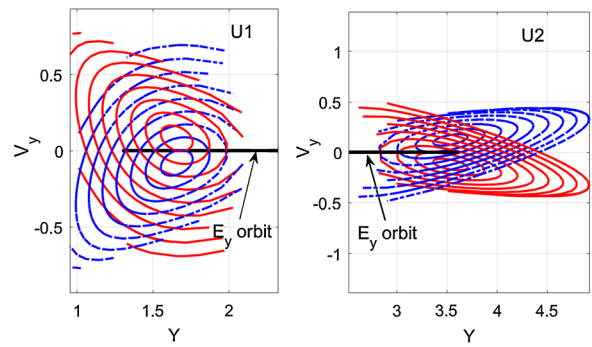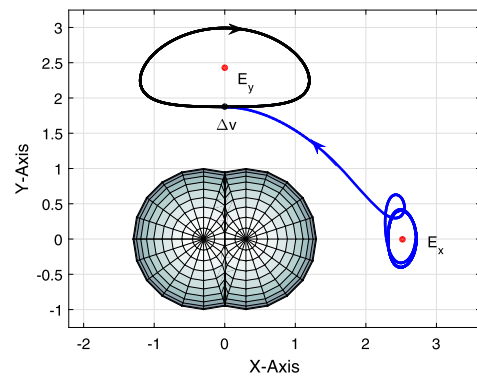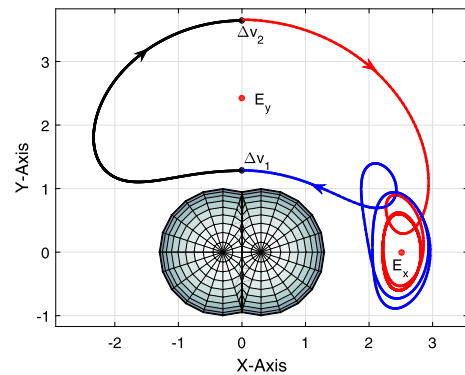
manifold-periodic orbit to stable manifold. Figure 23 shows an example.

4.5 Global transfer around a dumbbell-shaped body

Taking advantage of heteroclinic transfer between E_x and E_y, it is possible to complete the global transfer around a dumbbell-shaped body. Here, we design a series of reference transfer trajectories that can achieve transfers between different equilibria, and make a global observation about dumbbell-shaped bodies. The reference trajectories are shown in Fig. 24. Such trajectories consist of two periodic orbits around E_x and E_{-x}, denoted as P_1 and
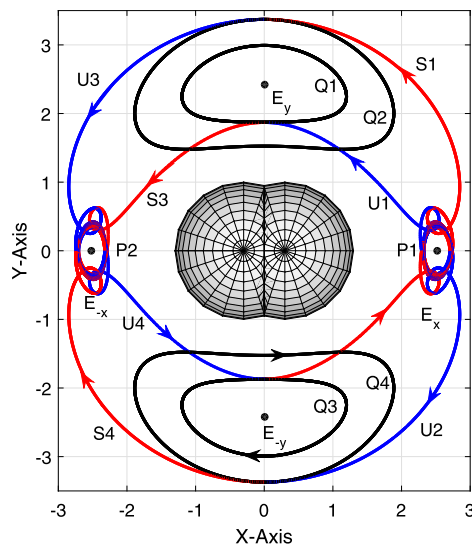
Fig. 24 Reference global transfer trajectory around a dumbbell-shaped body

P_2, their associated invariant manifolds, denoted S_1, S_2, S_3, S_4 and U_1, U_2, U_3, U_4, and four periodic orbits around E_y and E_{-y}, denoted Q_1, Q_2, Q_3, Q_4. The stable and unstable manifolds connect with Q_1, Q_2, Q_3, Q_4 in the plane $X = 0$, respectively.

Based on a reference transfer trajectory, several types of scenarios can be designed, including global mapping, a heteroclinic connection between E_{-y} and E_y, and a homoclinic connection for E_x, as shown in Fig. 25.

Figure 25(a) shows the transfer between Q_1 and Q_2; the transfer sequence is Q_1–S_3–P_2–U_3–Q_2. The reverse transfer is also available, but the transfer sequence becomes Q_2–S_1–P_1–U_1–Q_1. Figure 25(b) shows the transfer from Q_3 to Q_1; the spacecraft travels along Q_3–S_2–P_1–U_1–Q_1. Two impulses are required at the intersections of Q_3 and S_2 and U_1 and Q_1.

Figure 25(c) and (d) show two types of global mapping trajectories. The first uses the inner heteroclinic connection. The transfer sequence is P_1–U_1–Q_1–S_3–P_2–U_4–Q_3–S_2–P_1. The second uses the outer heteroclinic connection with sequence P_1–U_2–Q_4–S_4–P_2–U_3–Q_2–S_1–P_1. Both need four impulses at the intersections.

Figure 25(e) demonstrates the homoclinic connection for P_1, P_1–U_1–S_3–P_2–U_3–S_1–P_1. It can in fact be considered as two heteroclinic connections between E_x and E_{-x}. Taking advantage of the invariant manifolds, almost no energy is required during the transfer. Table 4 shows the velocity increment for each scenario. The parameter of the dumbbell-shaped body is assumed to be $R = 10$ km, the spin period is 6 h and the asteroid density is 3200 kg/m^3.

As shown in Table 4, due to the property of invariant manifolds, the total velocity increment for transfer is less than 5 m/s. These trajectories can be applied to future small-body exploration and provide references for design of reconnaissance orbits.

5 Conclusions

This paper investigates local and global motion in the vicinity of a rotating dumbbell-shaped body. Based on the polyhedron method,
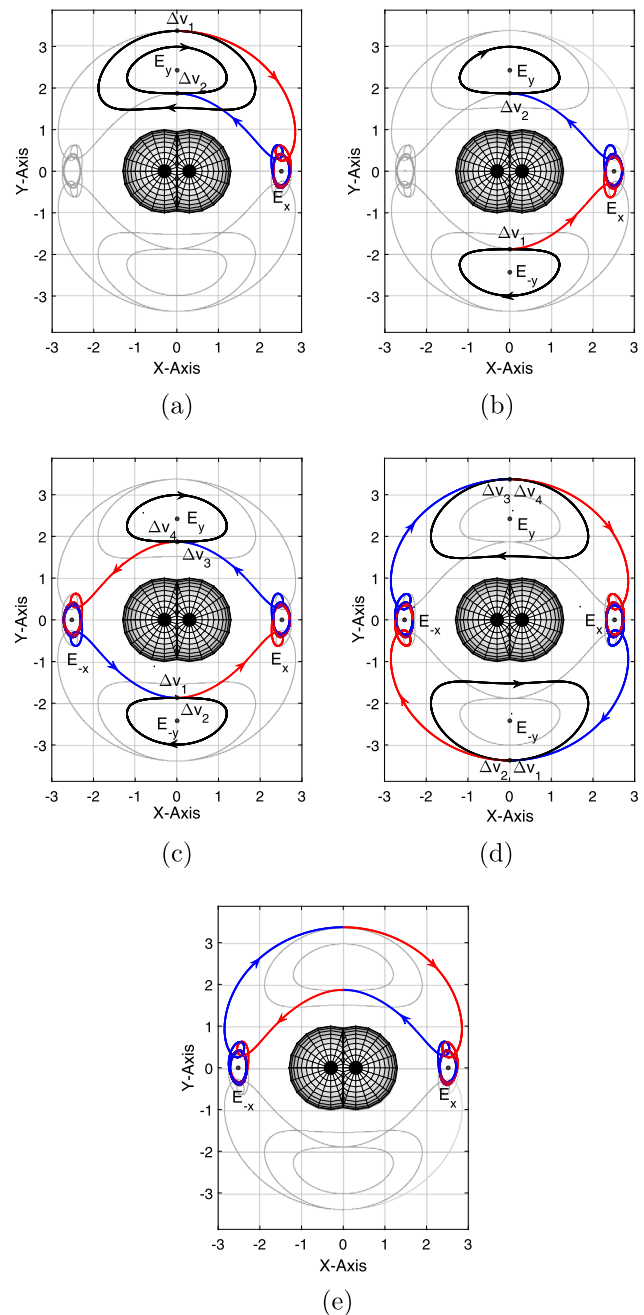

Fig. 25 Different transfer scenarios: (**a**) Transfer between orbits around E_y with different amplitudes; (**b**) Heteroclinic connection for E_y; (**c**) Global mapping by inner heteroclinic connection; (**d**) Global mapping by outer heteroclinic connection; (**e**) Homoclinic connection for E_x

a geometrical model of a dumbbell-shaped body is established, and the stability of equilibria are investigated with different parameters. The critical length-diameter ratios m_{cr} are calculated. Local motion around equilibria is analyzed. Based on linear perturbation equations, two, one and three types of periodic orbits are found around X-axis equilibria, unstable Y-axis equilibria and stable Y-axis equilibria, respectively. Using pseudo-arc-length continuation, a family of periodic orbits is generated. By introducing the bifurca-

Table 4 Transfer sequence and velocity increment for each scenario

Scenario	Transfer sequence	Velocity increment (m/s)
Transfer between orbits with different amplitudes	Q_1–S_3–P_2–U_3–Q_2	1.579
Heteroclinic connection for E_y	Q_3–S_2–P_1–U_1–Q_1	1.557
Global Mapping 1	P_1–U_1–Q_1–S_3–P_2–U_4–Q_3–S_2–P_1	3.114
Global Mapping 2	P_1–U_2–Q_4–S_4–P_2–U_3–Q_2–S_1–P_1	3.201
Homoclinic connection for E_x	P_1–U_1–S_3–P_2–U_3–S_1–P_1	/

tion method, more types of orbits are found around equilibria, such as 'Halo' orbits, 'Axial' orbits and multi-revolution orbits. Then, on the basis of invariant manifolds and Poincaré sections, global motion around the dumbbell-shaped body is studied. Four heteroclinic connections are found for equilibria along the X-axis. Low-energy transfers between different periodic orbits are constructed. Finally, several applications of global transfer trajectories are discussed that offer good options for reconnaissance orbits for future small-body exploration missions.

References

Alberti, A., Vidal, C.: Celest. Mech. Dyn. Astron. **98**(2), 75 (2007)

Campbell, E.T.: Bifurcations from families of periodic solutions in the circular restricted problem with application to trajectory design (1999)

Chappaz, L.P.R.: Dissertations Theses—Gradworks (2015)

Doedel, E.J., Romanov, V.A., Paffenroth, R.C., Keller, H.B., Dichmann, D.J., Galánvioque, J., Vanderbauwhede, A.: Int. J. Bifurc. Chaos **17**(8), 2625 (2007)

Feng, J., Noomen, R., Yuan, J.: Planet. Space Sci. **117**, 1 (2015)

Feng, J., Noomen, R., Visser, P., Yuan, J.: Adv. Space Res. **58**(3), 387 (2016)

Grebow, D.: MSAA Thesis, School of Aeronautics and Astronautics, Purdue University (2006)

Hudson, R.S., Ostro, S.J.: Science **263**(5149), 940 (1994)

Iooss, G., Joseph, D.D.: Arch. Ration. Mech. Anal. **66**(2), 135 (1977)

Jiang, Y., Baoyin, H.: J. Astrophys. Astron. **35**(1), 17 (2014)

Jiang, Y., Baoyin, H., Li, J., Li, H.: Astrophys. Space Sci. **349**(1), 83 (2014)

Jiang, Y., Yu, Y., Baoyin, H.: Nonlinear Dyn. **81**(1–2), 119 (2015)

Lara, M., Scheeres, D.J.: J. Astronaut. Sci. **50**(4), 389 (2002)

Li, X., Qiao, D., Cui, P.: Astrophys. Space Sci. **348**(2), 417 (2013)

Liu, X., Baoyin, H., Ma, X.: Astrophys. Space Sci. **333**(2), 409 (2011a)

Liu, X., Baoyin, H., Ma, X.: Astrophys. Space Sci. **334**(2), 357 (2011b)

Riaguas, A., Elipe, A., López-Moratalla, T.: Celest. Mech. Dyn. Astron. **81**(3), 235 (2001)

Scheeres, D.J.: Icarus **110**(2), 225 (1994)

Scheeres, D.J., Ostro, S.J., Hudson, R.S., Werner, R.A.: Icarus **121**(1), 67 (1996)

Wang, X.-Y., Gong, S.-P., Li, J.-F.: Acta Mech. Sin. **30**(3), 316 (2014)

Wang, X., Jiang, Y., Gong, S.: Astrophys. Space Sci. **353**(1), 105 (2015)

Werner, R.A., Scheeres, D.J.: Celest. Mech. Dyn. Astron. **65**(3), 313 (1996)

Yu, Y., Baoyin, H.: Mon. Not. R. Astron. Soc. **427**(1), 872 (2012a)

Yu, Y., Baoyin, H.: Astron. J. **143**(3), 160 (2012b)

Yu, Y., Baoyin, H.: Astrophys. Space Sci. **343**(1), 75 (2013)

Zeng, X., Jiang, F., Li, J., Baoyin, H.: Astrophys. Space Sci. **356**(1), 1 (2015)